Article

One-Step Hydrothermal Synthesis of 3D Interconnected rGO/In$_2$O$_3$ Heterojunction Structures for Enhanced Acetone Detection

Xiaoguang San [1], Yue Zhang [1], Lei Zhang [1], Guosheng Wang [1], Dan Meng [1,*], Jia Cui [1] and Quan Jin [2,*]

[1] College of Chemical Engineering, Shenyang University of Chemical Technology, Shenyang 110142, China; sanxiaoguang@syuct.edu.cn (X.S.); meat_d@163.com (Y.Z.); 15164038413@163.com (L.Z.); wgsh-lyc@163.com (G.W.); cuijiakj@163.com (J.C.)

[2] School of Materials Science and Engineering, Jilin University, Changchun 130012, China

[*] Correspondence: mengdan0610@hotmail.com (D.M.); qjin@jlu.edu.cn (Q.J.)

Abstract: Acetone detection is of great significance for environmental monitoring or diagnosis of diabetes. Nevertheless, fast and sensitive detection of acetone at low temperatures remains challenging. Herein, a series of rGO-functionalized three-dimensional (3D) In$_2$O$_3$ flower-like structures were designed and synthesized via a facile hydrothermal method, and their acetone-sensing properties were systematically investigated. Compared to the pure 3D In$_2$O$_3$ flower-like structures, the rGO-functionalized 3D In$_2$O$_3$ flower-like structures demonstrated greatly improved acetone-sensing performance at relatively low temperatures. In particular, the 5-rGO/In$_2$O$_3$ sensor with an optimized decoration exhibited the highest response value (5.6) to 10 ppm acetone at 150 °C, which was about 2.3 times higher than that of the In$_2$O$_3$ sensor (2.4 at 200 °C). Furthermore, the 5-rGO/In$_2$O$_3$ sensor also showed good reproducibility, a sub-ppm-level detection limit (1.3 to 0.5 ppm), fast response and recovery rates (3 s and 18 s, respectively), and good long-term stability. The extraordinary acetone-sensing performance of rGO/In$_2$O$_3$ composites can be attributed to the synergistic effect of the formation of p-n heterojunctions between rGO and In$_2$O$_3$, the large specific surface area, the unique flower-like structures, and the high conductivity of rGO. This work provides a novel sensing material design strategy for effective detection of acetone.

Keywords: In$_2$O$_3$ flower-like structures; rGO; composites; gas sensor; acetone

1. Introduction

Acetone, as a volatile organic compound (VOC), is widely used in industries and laboratories [1,2]. However, due to its volatility and toxicity, it is becoming a typical pollution gas and threatening our health. Long-term inhalation of acetone gas at concentrations over 173 ppm may cause serious health problems, such as headache, nausea, vomiting, and central nervous system anesthesia [3]. Additionally, acetone can be used as a biomarker for the diagnosis of type 1 diabetes. It has been found that the exhaled acetone concentration in diabetes patients (1.8 ppm) is significantly higher than that of healthy controls (0.9 ppm) [4]. Therefore, developing an effective sensor operating in a wide acetone concentration range is crucial for environmental monitoring or diagnosis of diabetes.

Recently, many kinds of sensors based on optical, electric, gravimetric transduction techniques, etc., have been developed for detecting VOCs [5,6]. Avramov et al. presented an optimization-mass-sensitive sensor using a surface acoustic wave (SAW)-based two-port resonator as a highly sensitive quartz crystal microbalance (QCM), which exhibited excellent VOC-sensing properties [7]. Kanawade et al. reported a new negative-axicon fiber-optic sensor platform, which exhibits many desirable characteristics for sensing various VOCs at room temperature [8]. However, how to reduce their production costs and limit of detection, and to utilize real-time detection, should be deeply studied. Resistive gas sensors

based on metal oxide semiconductors (MOX) are an important type of gas sensor due to their low production cost, ease of fabrication, and good long-term stability [9–11]. Until now, SnO_2 [12], In_2O_3 [13], Fe_2O_3 [14], ZnO [15], WO_3 [16], Co_3O_4 [17], CuO [18], V_2O_5 [19], MoO_3 [20], and other metal oxide semiconductors with micro/nanostructures have been extensively investigated for the detection of various gases. Among them, In_2O_3, owing to its wide band gap, high catalytic activity, and low resistivity, has proven to be an excellent n-type sensing material for detecting VOCs such as methanol, ethanol, formaldehyde, and acetone [21–26]. For example, Yoon et al. [22] synthesized In_2O_3 nanoparticles via a microwave-assisted hydrothermal technology, which showed high responsivity and selectivity to ethanol at 300 °C. Liu et al. [24] reported that Yb-doped porous In_2O_3 nanosheets exhibited excellent sensing performance for acetone. Zhao et al. [25] synthesized hierarchical In_2O_3 nanostructures via a simple hydrothermal method, which showed ultrafast response speed, excellent selectivity, and stability for formaldehyde. Nevertheless, the rapid and accurate detection of trace acetone using In_2O_3 at a low temperatures remains a great challenge and, thus, has been the focus of ongoing research.

In recent years, two-dimensional (2D) graphene-based nanomaterials, including graphene oxide (GO) and reduced graphene oxide (rGO), have been extensively studied as potential gas-sensing materials due to their high specific surface area, outstanding electrical properties, abundant functional groups, and excellent charge-carrier mobility. [27,28]. Unfortunately, the low sensing response, slow response and recovery rates, and poor selectivity of graphene-based sensing materials limit their practical application. Taking into account the advantages of GO/rGO and MOX, the construction of GO/MOX or rGO/MOX hybrid micro–nanostructures is considered an effective way to enhance gas-sensing performances [29–32]. To date, a number of GO/MOX or rGO/MOX hybrids—such as SnO_2/rGO, rGO/Co_3O_4, rGO/WO_3, rGO/In_2O_3, ZnO/rGO, etc.—have been prepared, and demonstrate good sensing performance in detecting both oxidizing and reducing gases [33–38]. For instance, Meng et al. [33] prepared rGO/Co_3O_4 nanocomposites via a one-step hydrothermal method, which could detect ppb level xylene. Cao et al. [37] constructed ZnO/rGO heterostructures through a chemiresistive approach, exhibiting good linearity in the ppb range, high selectivity, and good long-term stability for NO_2. Inspired by the above results, it is hoped that researchers will be able to uniformly distribute 3D In_2O_3 flower-like structures on 2D rGO sheets via a feasible and economic route for developing an acetone gas sensor with high performance.

In the present study, well-designed rGO-functionalized 3D In_2O_3 flower-like structures were constructed via a one-step hydrothermal route, and their acetone-sensing properties were systemically investigated. It was clear that the optimized rGO/In_2O_3 composites demonstrated significantly enhanced acetone-sensing performance in comparison to pure In_2O_3 flower-like structures. The remarkably improved sensing performance of rGO/In_2O_3 composites can be attributed to the synergistic effect of the formation of p-n heterojunctions between rGO and In_2O_3, the large specific surface area, the unique flower-like structures, and the high conductivity of rGO. This work provides a novel sensing material for effective detection of acetone.

2. Experimental

2.1. Materials and Synthesis

Graphene oxide (GO) was synthesized via Hummers' method using graphite flakes as raw materials [39]. Then, the obtained GO was dispersed into ethanol and ultrasonically treated for 1.5 h to obtain a uniform 0.5 mg/mL GO dispersion. The rGO-functionalized 3D In_2O_3 flower-like structures were synthesized by a one-step hydrothermal route, which is schematically illustrated in Figure 1. Typically, 0.13 g of indium nitrate ($In(NO_3)_3 \cdot 4.5H_2O$), 1 g of urea (H_2NCONH_2), and 0.26 g of sodium dodecyl sulfate ($CH_3(CH_2)_{11}OSO_3Na$) were dissolved in 20 mL of distilled water, and then stirred for 0.5 h to obtain a transparent solution. After that, a certain volume of GO solution was added to the above solution and stirred at room temperature for 0.5 h to form a well-dispersed suspension with different

mass ratio of rGO/In$_2$O$_3$. Diverse volumes of ethanol were added to the above mixtures until the total volume was 40 mL. Subsequently, the mixed solution was transferred into a 50 mL Teflon-lined stainless steel autoclave and then heated in an oven at 160 °C for 3 h, in which structural modification of the In$_2$O$_3$ flower-like structures and the reduction of GO occurred simultaneously. After the reaction, the precipitate was collected by centrifugation and washed several times with distilled water and ethanol to remove the impurities, and then dried at 60 °C for 8 h. Finally, the obtained precursor was annealed in a tube furnace at 400 °C for 2 h under a nitrogen atmosphere. In our experiment, the mass ratio of GO in the composites was 1 wt%, 3 wt%, 5 wt%, 7 wt%, and 10 wt%, respectively; consequently, the rGO/In$_2$O$_3$ composites were labeled as 1-rGO/In$_2$O$_3$, 3-rGO/In$_2$O$_3$, 5-rGO/In$_2$O$_3$, 7-rGO/In$_2$O$_3$, and 10-rGO/In$_2$O$_3$, respectively. For comparison, the pure In$_2$O$_3$ flower-like structures were synthesized individually by the same procedure without the addition of GO.
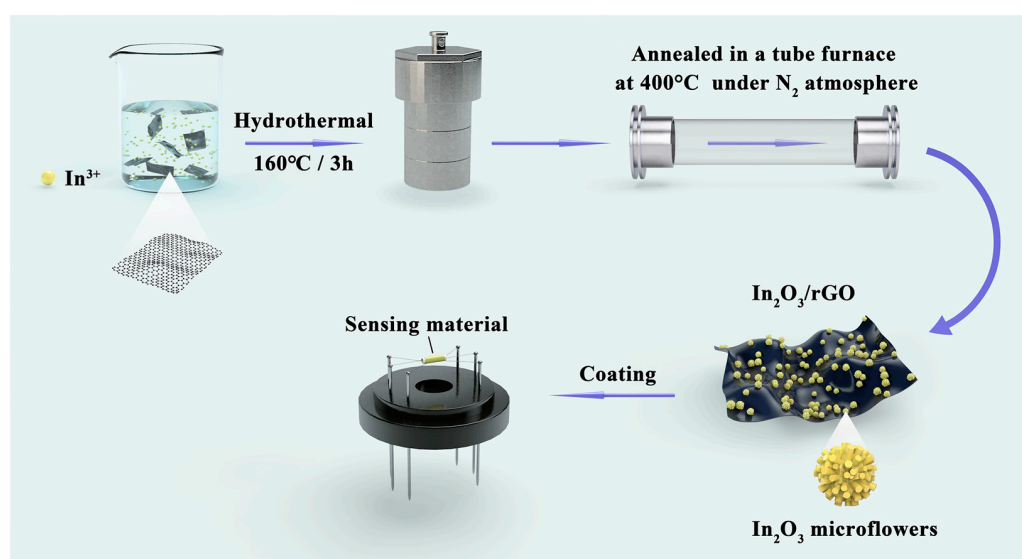

Figure 1. The schematic of the synthesis process of the rGO/In$_2$O$_3$ composites.

2.2. Materials Characterization

The crystal structure of the rGO/In$_2$O$_3$ composites was characterized by X-ray diffraction (XRD, Shimadzu XRD-6100). The surface morphologies of the rGO/In$_2$O$_3$ composites were analyzed using field-emission scanning electron microscopy (FE-SEM, ZEISS Ultra Plus). The internal structure of the rGO/In$_2$O$_3$ composites was further observed by high-resolution transmission electron microscopy (HRTEM) on a TEM system (JEOL, JEM-2100F). The distribution of elements was obtained by energy-dispersive spectrometry (EDS) mapping on a JEOL-JEM-2100F TEM. Then, the specific surface area and pore size distribution were analyzed by the Brunauer–Emmet–Teller (BET, Quantachrome Autosorb1-C) method and the Barrett–Joyner–Halenda (BJH) model. In addition, the surface compositions and states of the rGO/In$_2$O$_3$ composites were investigated by X-ray photoelectron spectroscopy (XPS, JEOL JPS9010MC).

2.3. Sensor Fabrication and Measurement

The gas sensor was fabricated as follows: First, an appropriate amount of rGO/In$_2$O$_3$ or pure In$_2$O$_3$ powder was ground and mixed with ethanol to form a homogeneous slurry, which was then coated on the outer surface of the ceramic tube electrode. The ceramic tube electrode was composed of four Pt wires and two Au electrodes spaced 6 mm apart. After forming a sensing film by evaporating ethanol, a Ni-Cr heated wire was passed through the hollow ceramic tube, and the Ni–Cr wire and Pt wires were subsequently welded on a hexagonal base to fabricate the gas sensor, as shown in Figure 1. Finally, the gas sensor was

placed on a TS60 desktop (Winsen Electronics Co., Ltd., Zhengzhou, China) and aged at 400 °C for 48 h to ensure the stability of the sensing device.

Gas-sensitive measurements of the fabricated sensors were performed on a commercial WS-30A system (Winsen Electronics Co., Ltd., Zhengzhou, China) under static laboratory conditions (temperature: 20–25 °C; relative humidity (RH): 20–35%). To obtain the target gas, corresponding volumes of testing liquid were injected into the testing chamber (18 L) using a microsyringe and then evaporated to record and analyze the change in current. The following equation can be used to calculate the target gas concentration:

$$C = \frac{22.4 \times \varphi \times \rho \times V}{V_{chamber} \times M} \qquad (1)$$

where V is the volume (μL) of the injected testing liquid, $V_{chamber}$ is the volume (L) of the testing chamber, C is the vapor concentration (ppm) of the target gas, M is the molar mass (g/mol) of the target gas, ρ is the density (g/mL) of the testing liquid, and φ is the volume fraction of the target gas. After the gas-sensing response reached a constant value, the testing gas was released by opening the chamber. Herein, the sensing response to different target gases was defined as Ra/Rg, where Ra and Rg are the resistance of the sensors in air and target gases, respectively. Moreover, the response and recovery time were calculated as the time required to achieve 90% change in resistance after the sensor was exposed to the target gas and fresh air, respectively.

3. Results and Discussion

3.1. Structural and Morphological Characteristics

Figure 2 illustrates the XRD patterns of the In_2O_3 and rGO/In_2O_3 composites. In_2O_3 displayed perfect crystallinity, and the diffraction peaks that appeared at 2θ values of 21.5, 30.6, 35.5, 37.7, 39.8, 45.7, 51.0, and 60.7° were ascribed to the (211), (222), (400), (411), (420), (431), (440), and (622) planes of the cubic phase In_2O_3 (JCPDS No. 06-0416), respectively. As for the rGO/In_2O_3 composites, all of the diffraction peaks were consistent with In_2O_3, indicating that introducing rGO to In_2O_3 has no obvious influence on the phase. Here, there were no obvious diffraction peaks of rGO in the patterns, which might have been due to the low content of rGO in the composites and the low diffraction intensity of rGO. In addition, no other impurity peaks were observed, confirming their high purity.

The morphology of the In_2O_3 and rGO/In_2O_3 composites was investigated by FE-SEM, as shown in Figure 3. The low-magnification FE-SEM image (Figure 3a) clearly demonstrates numerous 3D In_2O_3 flower-like structures with diameters ranging from 1 to 2 μm. These flower-like structures were composed of nanorods with diameters of 100 to 300 nm (Figure 3b), and a specific spacing between each nanorod was clearly observed, illustrating their porous structures. From the FE-SEM images of the 1-rGO/In_2O_3 composites (Figure 3c,d), it is clear that the 3D In_2O_3 flower-like structures remained, and some of them uniformly attached to the surface of the rGO sheets, forming a 3D interconnected structure, and thereby contributing to enhancement of the sensing properties. Moreover, the crumpled rGO sheets with many folds and wrinkles exhibited a clean and transparent film. The morphologies of the 3-rGO/In_2O_3, 5-rGO/In_2O_3, 7-rGO/In_2O_3, and 10-rGO/In_2O_3 composites were similar to that of the 1-rGO/In_2O_3 composites, as shown in Figure 3e–l. It is worth noting that there were no significant changes in the size and the uniformity of the In_2O_3 flower-like structures. Additionally, with increasing the mass ratio of rGO, many ultrathin layered structures were observed, and some of them tend to aggregate with one another, which is unfavorable for the gas-sensing property.
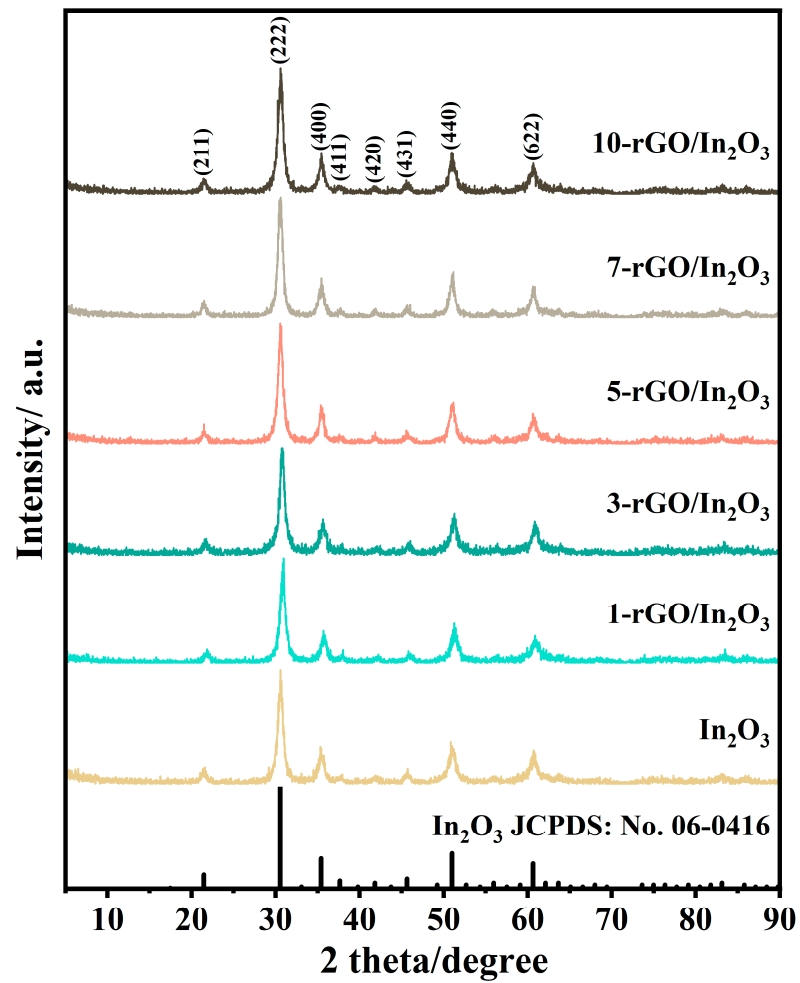
Figure 2. XRD patterns of the pure In_2O_3, 1-rGO/In_2O_3, 3-rGO/In_2O_3, 5-rGO/In_2O_3, 7-rGO/In_2O_3, and 10-rGO/In_2O_3.
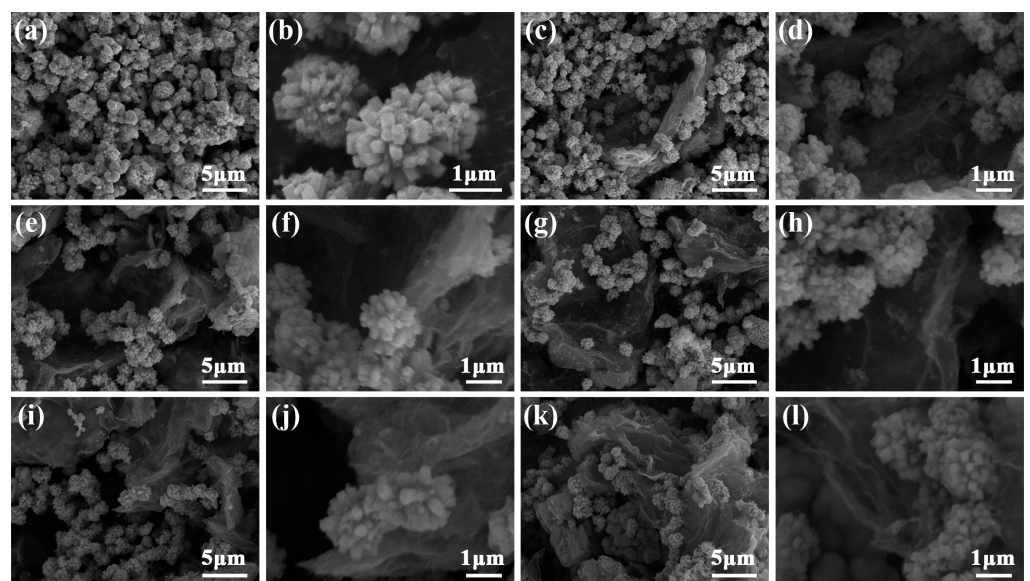

Figure 3. FE-SEM images of (**a**,**b**) In_2O_3, (**c**,**d**) 1-rGO/In_2O_3, (**e**,**f**) 3-rGO/In_2O_3, (**g**,**h**) 5-rGO/In_2O_3, (**i**,**j**) 7-rGO/In_2O_3, and (**k**,**l**) 10-rGO/In_2O_3.

The In_2O_3 flower-like structures attached on the rGO sheets were also clearly observed in the TEM image (Figure 4a), consistent with the FE-SEM image. The HRTEM image (Figure 4b) shows that 0.292 and 0.179 nm lattice spacings fit well with the (222) and (440) crystal planes of In_2O_3 [40]. Meanwhile, the EDS elemental mappings (Figure 4c–e) clearly indicate that the In, O, and C are uniformly distributed throughout the whole region, further implying the formation of the rGO/In_2O_3 composites. Taking the results of the FE-SEM and TEM observations into account, it is possible to conclude that the rGO/In_2O_3 composites were successfully prepared.
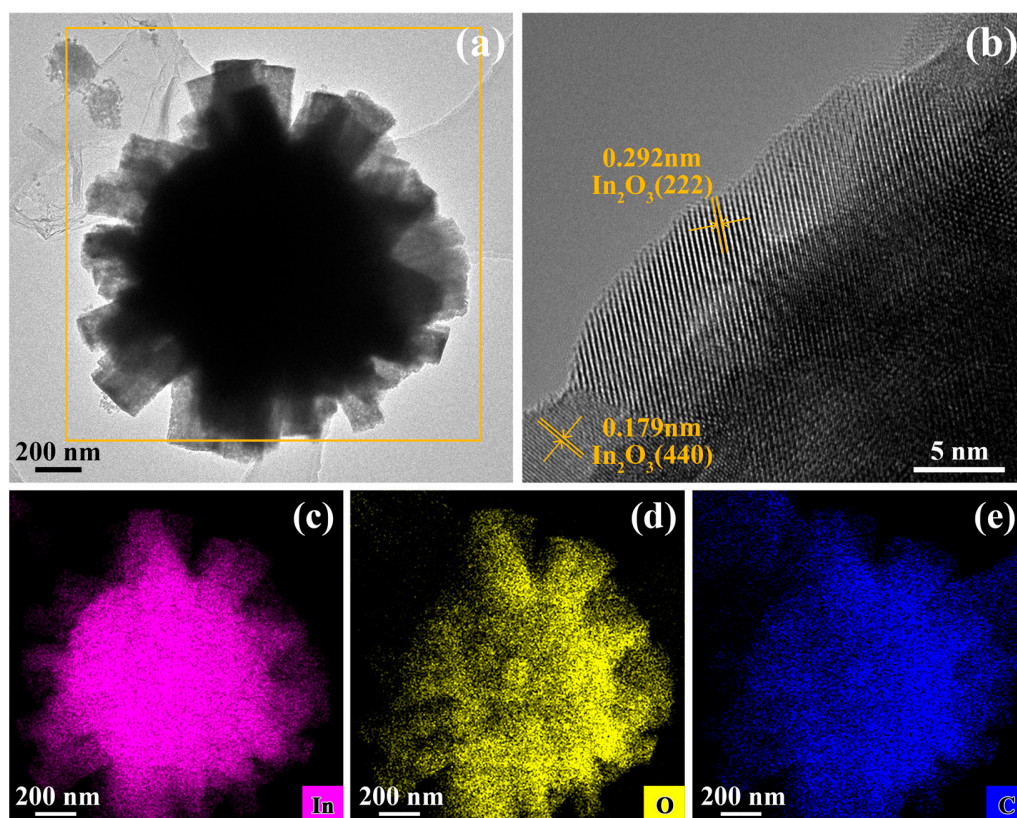

Figure 4. (**a**) TEM image, (**b**) high-resolution TEM image, and (**c–e**) its corresponding elemental mapping of $5\text{-}rGO/In_2O_3$ composites.

XPS analysis was performed to investigate the surface composition and chemical state of the $5\text{-}rGO/In_2O_3$ composites. The survey spectra shown in Figure 5a show that the rGO/In_2O_3 composites were mainly composed of In, O, and C, confirming the successful preparation of the rGO/In_2O_3 composites. The In 3D symmetric peaks with binding energy of 444.83 eV and 452.37 eV (Figure 5b) were attributed to $In3d_{3/2}$ and $In3d_{5/2}$, respectively, indicating the existence of In^{3+} in the composites [41,42]. Figure 5c depicts three different chemical states of O 1s peaks at 530.30 eV, 531.84 eV, and 533.36 eV, corresponding to lattice oxygen (O_L), oxygen vacancies (O_V), and the surface hydroxyl groups (O_{OH}), respectively [43]. As for the C1s XPS spectrum of the composites (Figure 5d), it can be decomposed into three peaks at 284.60 eV, 285.55 eV, and 289.64 eV, which correspond to C=C–C, C–O/C–In, and C=O bonds in the rGO/In_2O_3 composites, respectively [44]. The above results further demonstrate the successful preparation of rGO/In_2O_3 composites.

The nitrogen adsorption–desorption measurements were performed to further confirm the specific surface area and porous structures of the samples. From Figure 6a,b, it can be seen that both of the curves are recognized as type IV isotherms with obvious hysteresis loops, indicating the formation of mesopores in the samples [45]. The specific surface area of the In_2O_3 and $5\text{-}rGO/In_2O_3$ composites was calculated to be 35.4 and 64.6 m^2/g, respectively. Obviously, the surface area of the $5\text{-}rGO/In_2O_3$ composites was significantly

higher than that of pure In_2O_3, due to the introduction of rGO. The pore size distribution diagram (inset) shows that the pore size of the In_2O_3 and rGO/In_2O_3 composites was predominantly concentrated at 8.129 and 6.124 nm, respectively, indicating the existence of many mesopores in the products. As a result, the rGO/In_2O_3 composites possess a higher specific surface area and a porous structure, which is advantageous for effective gas absorption and diffusion, contributing to the improved sensing performance.
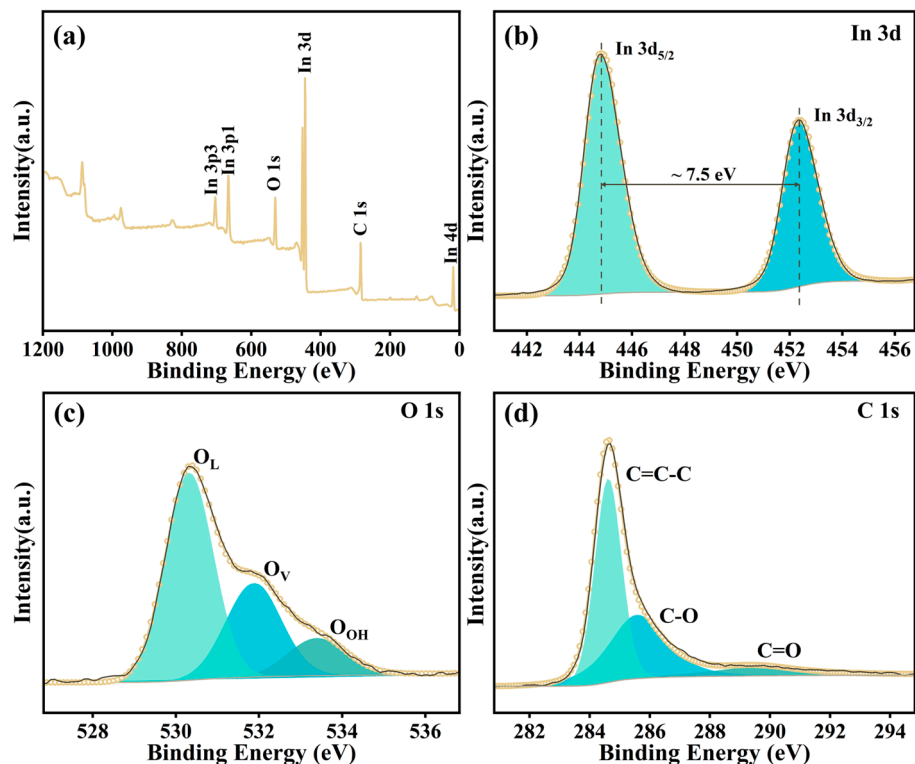

Figure 5. (**a**) Survey XPS spectra of 5-rGO/In_2O_3, (**b**) XPS spectrum of In, (**c**) XPS spectrum of O, and (**d**) XPS spectrum of C.
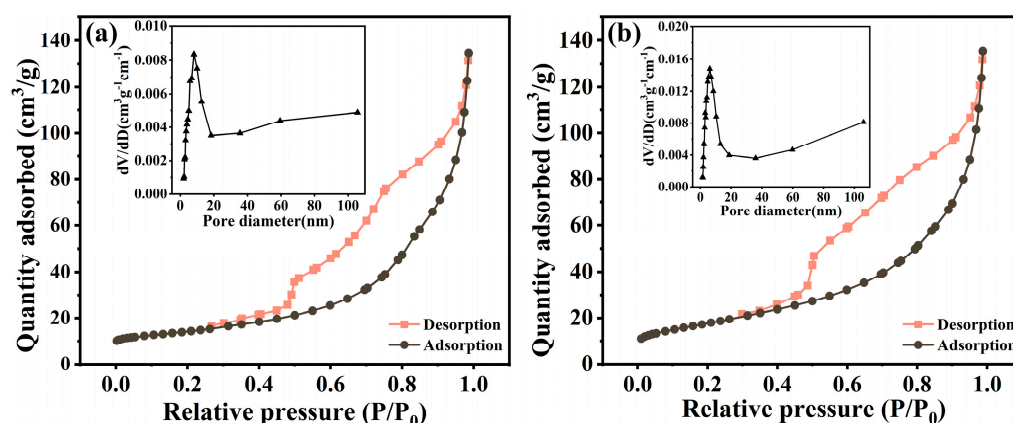
Figure 6. Typical N_2 adsorption–desorption isotherm and pore size distribution plots (inset) of (**a**) In_2O_3 and (**b**) 5-rGO/In_2O_3.

3.2. Gas Sensing Performance

In order to investigate the effects of rGO mass ratios on the sensing performance of In_2O_3 sensors, we fabricated gas sensors made of In_2O_3 flower-like structures and rGO-functionalized In_2O_3 flower-like structures, and tested their sensing performance. It is well known that the operating temperature has a significant impact on the sensing properties of

gas sensors. In order to evaluate the effect of operating temperature on the sensing ability and obtain the optimal operating parameters, the sensing response to 10 ppm acetone was first examined in the temperature range of 50 to 250 °C, as shown in Figure 7a. It was clearly found that all response curves showed an "increase-maximum-decrease" trend. This response pattern can be mostly attributed to the kinetic and thermodynamic factors of gas adsorption and desorption on the surface of the sensing materials [46,47]. The optimal operating temperature of the In_2O_3 sensor was 200 °C, while it was 150 °C for all rGO/In_2O_3 sensors, indicating that introducing rGO to In_2O_3 flower-like structures can effectively reduce the optimal operating temperature. The corresponding response values of sensors based on composites with different rGO mass ratios at their optimal operating temperatures are summarized in Figure 7b. Obviously, all rGO/In_2O_3 sensors except the $10\text{-}rGO/In_2O_3$ sensor exhibited higher responses than that of the In_2O_3 sensor at their optimal operating temperature. In particular, the $5\text{-}rGO/In_2O_3$ sensor exhibited the highest response value of 5.6, which was about 2.3 times higher than that of the In_2O_3 sensor (2.4 at 200 °C). This suggests that introducing an appropriate amount of rGO not only effectively reduces the optimal operating temperature, but also significantly improves the acetone-sensing response. Herein, considering the high acetone-sensing performance of the $5\text{-}rGO/In_2O_3$ sensor, this sensor was chosen for further study of other characteristics at its optimal operating temperature of 150 °C.
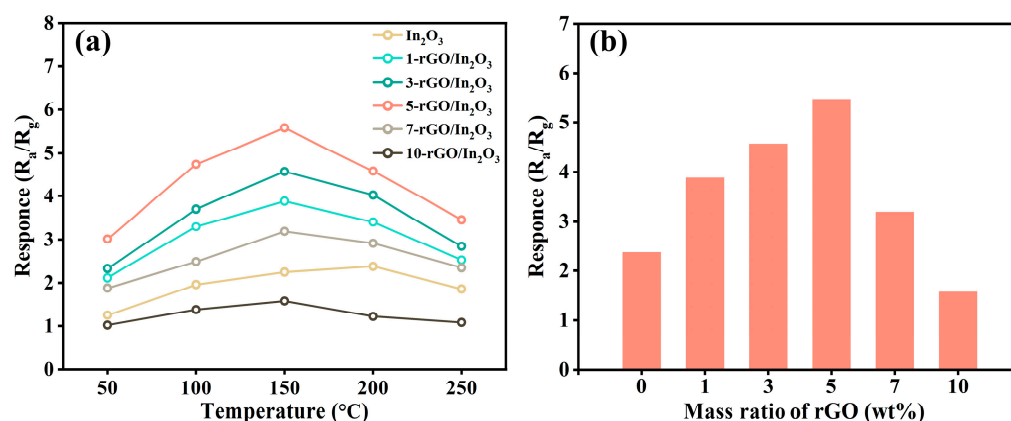

Figure 7. (**a**) The sensing response to 10 ppm acetone at various operating temperatures. (**b**) Correlations between the sensing response to 10 ppm acetone at the optimal operating temperature and rGO mass ratios.

The transient response and recovery curves of the $5\text{-}rGO/In_2O_3$ sensor to different concentrations of acetone (0.5 to 100 ppm) at 150 °C are displayed in Figure 8a. As can be seen, the resistance dropped rapidly upon exposure to acetone, and quickly returned to its initial resistance value after removing the acetone, demonstrating typical n-type semiconductor sensing features. Moreover, the response and recovery behavior repeated very well, revealing good reversibility and stability. It should be noted that the resistance change is still considerable when exposed to 0.5 ppm acetone, indicating that the detection limit could extend down to sub-ppm levels. To exhibit its response performance, the corresponding response values of the $5\text{-}rGO/In_2O_3$ sensor as a function of acetone concentration are illustrated in Figure 8b. Apparently, the responses value rapidly increases with increasing acetone concentration in the range of 0.5 ppm to 10 ppm. However, when the concentration is above 10 ppm, the rate of increase in the response value tends to slow down due to the high coverage of acetone molecules on the surface of the sensing material. Moreover, the sensor has an obvious response to sub-ppm levels of acetone (0.5 ppm, 1.3). Figure 8c presents the transient response and recovery curve of the $5\text{-}rGO/In_2O_3$ sensor when exposed to 10 ppm acetone at 150 °C. The response and recovery times were calculated to be 3 s and 18 s, respectively, revealing quick response and recovery characteristics as the acetone gas is injected and exhausted. As for practical gas-sensing applications,

selectivity and stability are of great importance. Figure 8d displays the sensing response of the 5-rGO/In$_2$O$_3$ sensor to 10 ppm potential interfering gases (i.e., ethanol, methanol, formaldehyde, trimethylamine, and ammonia) at 150 °C. The sensor exhibited a higher response to acetone compared to other interfering gases, indicating its good selectivity. Additionally, the response values of the 5-rGO/In$_2$O$_3$ sensor to different concentrations (0.1 ppm, 0.5 ppm, and 10 ppm) did not decrease significantly after the 30-day testing period (Figure 8e), implying its good long-term stability. As shown in (Figure 8f), the responses of the 5-rGO/In$_2$O$_3$ sensor to 10 ppm acetone at 150 °C showed slight decreases under relative humidity (RH) ranging from 25% to 45%, and an obvious decrease at RH levels above 75%. This decrease in sensing responses can be ascribed to the adsorption competition between oxygen species and water molecules on the sensor surface [48]. Furthermore, the acetone-sensing performance in this work was compared with the previous literature, as summarized in in Table 1. Compared with the previous reports, our 5-rGO/In$_2$O$_3$ sensor had the noticeable advantages of high response values at a relatively low operating temperature, a sub-ppm-level detection limit, and short response and recovery times, suggesting its potential application as an acetone sensor. However, there are also some drawbacks in this work. For example, how to overcome the influence of water vapor on the gas-sensing characteristics at high RH levels (>75%) should be further investigated for the diagnosis of diabetes in real applications. Moreover, the unsatisfactory selectivity should be also improved by coating functional materials as a "selective gas filter" on the sensing layer surface in future works.
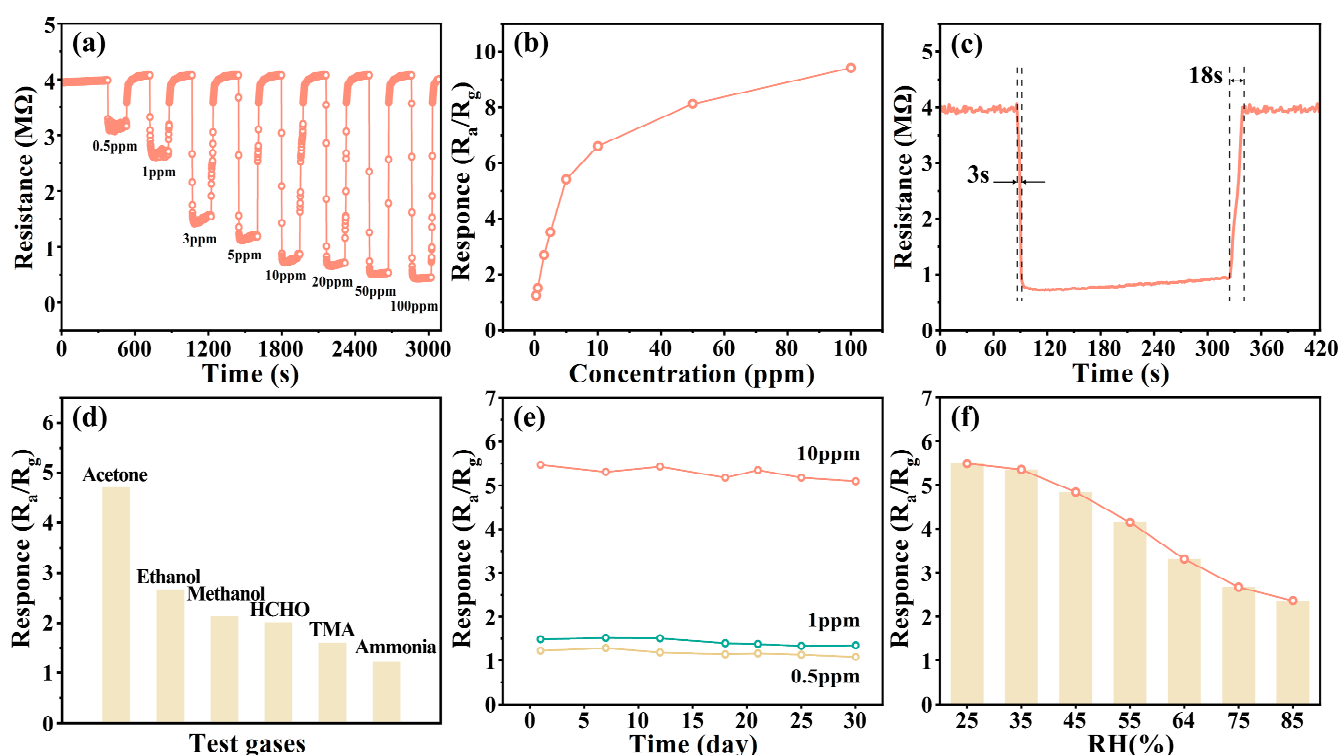
Figure 8. (**a**) The transient response and recovery curves for acetone in the range of 0.5–100 ppm. (**b**) The corresponding sensing response as a function of acetone concentration. (**c**) The dynamic sensing transients to 10 ppm acetone. (**d**) The selectivity and (**e**) long-term stability for 0.5/1/10 ppm acetone. Here, the sensor is made of 5-rGO/In$_2$O$_3$ composites, and the operating temperature is 150 °C. (**f**) The sensing responses to 10 ppm acetone under different relative humidity levels at 150 °C.

Table 1. Comparison of sensing properties for acetone detection.

Sensing Materials	Temp. (°C)	Con. (ppm)	Response (Ra/Rg)	Res./Rec. Time (s)	Detection Limit	Ref.
ZnO/NPC	350	100	25.47	3/150	1 ppm	[49]
α-Fe$_2$O$_3$-24	220	100	46.6	1/15	1 ppm	[50]
Ag-TiO$_2$ nanobelts	260	500	28.25	6/8	10 ppm	[51]
Ag@CuO-TiO$_2$	200	100	6.2	9/56	1 ppm	[52]
WO$_3$	200	100	28.7	3/113	2 ppm	[53]
SnO$_2$ nanotubes	325	100	20.3	66/15	5 ppm	[54]
In$_2$O$_3$	200	10	2.37	8/44	1 ppm	This work
5-rGO/In$_2$O$_3$	150	10	5.57	3/18	0.5 ppm	This work

3.3. Acetone-Sensing Mechanism

Generally, for chemiresistive gas sensors, the sensing characteristics can be attributed to the resistance variation induced by the adsorption and desorption of gas molecules on the surface of the sensing materials, along with the surface redox reaction [55]. For the In$_2$O$_3$ sensor, numerous oxygen molecules in the air atmosphere are adsorbed on the surface of the sensing film, and capture free electrons from the In$_2$O$_3$ conduction band, forming chemisorbed oxygen species (O$_2^-$ O$^-$ and O^{2-}) via the following reactions [56]:

$$O_{2(ads)} + e^- \rightarrow O_2^-{}_{(ads)} \tag{2}$$

$$O_2^-{}_{(ads)} + e^- \rightarrow 2O^-{}_{(ads)} \tag{3}$$

$$O^-{}_{(ads)} + e^- \rightarrow O^{2-}{}_{(ads)} \tag{4}$$

Consequently, an electron deletion layer is created at the surface of In$_2$O$_3$, leading to a relatively high resistance state. As the reducing gas (acetone) is introduced, redox reactions between acetone molecules and the chemisorbed oxygen species take place, and then the electrons captured by oxygen molecules are released back into the In$_2$O$_3$ conduction band. In this process, the electron depletion layer becomes narrow and, thus, the resistance of the sensing materials decreases, ultimately generating a sensing signal. The related reactions are listed as follows [57]:

$$CH_3COCH_3 \text{ (gas)} \rightarrow CH_3COCH_3 \text{ (ads)} \tag{5}$$

$$CH_3COCH_3 \text{ (ads)} + 4O_2^- \text{ (ads)} \rightarrow 3CO_2 + 3H_2O + 4e^- \tag{6}$$

$$CH_3COCH_3 \text{ (ads)} + 8O^- \text{ (ads)} \rightarrow 3CO_2 + 3H_2O + 8e^- \tag{7}$$

Compared to the In$_2$O$_3$ sensor, the rGO/In$_2$O$_3$ sensor shows a significant improvement in sensing performance, which can be attributed to the following factors (Figure 9): First of all, the formation of a p-n heterojunction at the interface between n-type In$_2$O$_3$ and p-type rGO is one of the main factors improving the sensors' performances [58]. When In$_2$O$_3$ and rGO contact one another, the electrons flow from the n-type In$_2$O$_3$ with low work function to the p-type rGO with high work function until the Fermi energy level reaches equilibrium [59]; thus, a potential barrier is created at the heterojunctions. Consequently, two different depletion layers coexist in the rGO/In$_2$O$_3$ composites: one is the depletion layer formed by the adsorption of oxygen molecules at the surface of In$_2$O$_3$, and the other is created at the interface between rGO and In$_2$O$_3$ (p-n heterojunctions). As a consequence, the expanded depletion layer and potential barrier simultaneously lead to a high resistance state. The increase in the rGO/In$_2$O$_3$ composite's resistance is also confirmed by our experimental results. As shown in Figure 9d, the resistance value of the 5-rGO/In$_2$O$_3$ sensor is much higher than that of the In$_2$O$_3$ sensor throughout the whole temperature range, indicating that the formation of p-n heterojunctions contributes to raising the resistance value. Upon exposure to acetone, the local heterojunctions between rGO sheets and In$_2$O$_3$ flower-like structures offer additional resistance modulation by altering potential barriers and two electron depletion layers. According to the definition of the sensor response (S = Ra/Rg),

the total resistance of the rGO/In$_2$O$_3$ composites could be distinctly changed, inducing significant enhancement of the sensing response. Moreover, the formation of rGO/In$_2$O$_3$ heterojunctions can also generate more active sites, such as including point defects and vacancies, which further adds to the increase in the sensing response [60]. The second aspect originates from the coupling interaction between rGO sheets and In$_2$O$_3$ flower-like structures, which creates a 3D interconnected structure and plays an important role in gas-sensing applications. The intercalation of rGO sheets can prevent the agglomeration of In$_2$O$_3$ flower-like structures, which not only significantly increase the specific surface area for more efficient gas adsorption reactions, but also offer more pathways for facilitating gas diffusion and transport, thus improving the sensing performance [61]. It has already been confirmed from BET analysis that the specific surface area of the rGO/In$_2$O$_3$ composites is higher than that of the In$_2$O$_3$ flower-like structures. In addition, rGO, owing to its quantity of dangling bonds and surface defects, is favorable for the adsorption of target gases [62]. Meanwhile, the unique In$_2$O$_3$ flower-like structures also facilitate the operative access of gases to the surface. These characteristics greatly contribute to enhancing the sensing response and recovery properties of rGO/In$_2$O$_3$ composites. Thirdly, the excellent electron conductivity of rGO is a positive factor for the enhanced sensing performances. From the FE-SEM images, it can be seen that the rGO sheets disperse adequately on the composites, and could act as an electron transfer layer accelerating the electronic transmission rate at the interfaces between In$_2$O$_3$ and rGO. This is helpful for reducing the optimal temperature and improving repeatability and stability. Based on the above discussion, the combination of In$_2$O$_3$ and rGO contributes to the superior sensing properties, including high response at relatively low temperatures, good stability, and fast response and recovery rates, demonstrating potential application for detecting acetone.
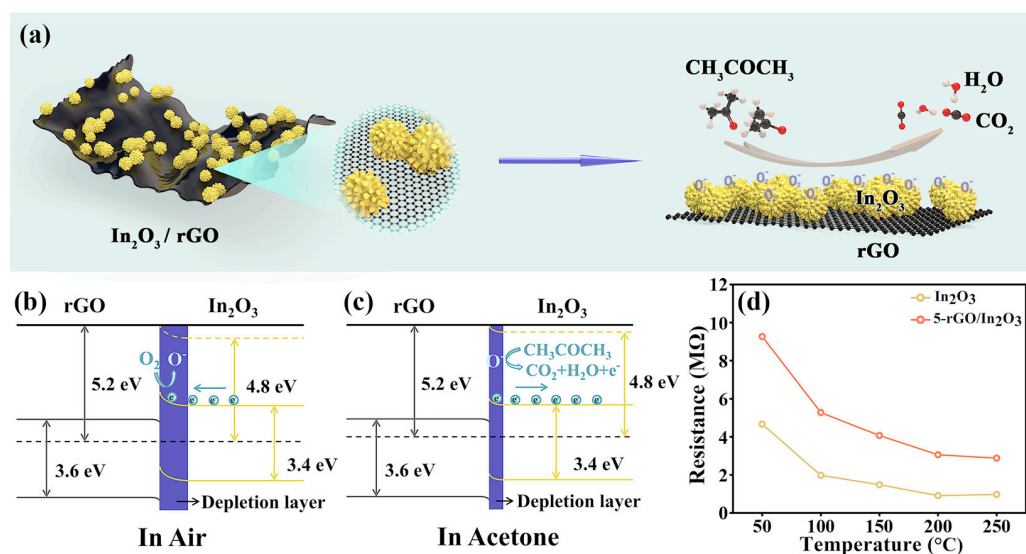

Figure 9. (**a**) Schematic diagram of the mechanism of the acetone gas-sensing process of the rGO/In$_2$O$_3$ composites. (**b**,**c**) Schematics of energy band diagrams of rGO/In$_2$O$_3$ heterojunctions. (**d**) The resistance of the sensors in air as a function of operating temperature.

4. Conclusions

In summary, a series of well-designed 3D interconnected rGO/In$_2$O$_3$ heterojunction structures were successfully constructed using a simple hydrothermal method. The FE-SEM and TEM analyses showed that In$_2$O$_3$ flower-like structures with sizes of 1–2 μm uniformly attached on the surface of the rGO sheets. Both the TEM-EDS and XPS results demonstrated the existence of In, O, and C, revealing the successful preparation of the rGO/In$_2$O$_3$ composites. In addition, the BET surface area of the 5-rGO/In$_2$O$_3$ composites (64.6 m^2/g) was significantly higher than that of pure In$_2$O$_3$ (35.4 m^2/g), implying their better sensing properties. As a result, the rGO/In$_2$O$_3$ composites achieved much better acetone-sensing

properties compared to pure In_2O_3 flower-like structures at the relatively low temperature of 150 °C. Specifically, the 5-rGO/In_2O_3 composites exhibited the highest response value of 5.6 to 10 ppm acetone, which was around 2.3 times higher than that of the In_2O_3 flower-like structures (2.4 at 200 °C). Furthermore, they also displayed good reproducibility, a sub-ppm-level detection limit (1.3 to 0.5 ppm), a fast response/recovery rate (3/18 s), and good long-term stability. The large advancement for rGO/In_2O_3 composites in acetone-sensing performance can be attributed to the synergistic effect of the formation of p-n heterojunctions between rGO and In_2O_3, the large specific surface area and unique flower-like structure, and the high conductivity of rGO. This work not only developed a high-performance gas sensor to detect acetone, but also provides a novel strategy to enhance the sensing performance for MOX gas-sensing materials by reasonably utilizing the synergistic effect of structure and components.

Author Contributions: Conceptualization, Y.Z.; data curation, Y.Z. and J.C.; formal analysis, Y.Z., L.Z., G.W., D.M. and J.C.; funding acquisition, X.S.; investigation, Y.Z.; methodology, X.S., Y.Z. and D.M.; project administration, X.S., D.M. and Q.J.; resources, L.Z. and G.W.; supervision, D.M. and Q.J.; validation, X.S.; visualization, X.S. and Y.Z.; writing—original draft, Y.Z.; writing—review & editing, X.S., D.M. and Q.J. All authors have read and agreed to the published version of the manuscript.

Institutional Review Board Statement: Not applicable.

Informed Consent Statement: Not applicable.

Data Availability Statement: Not applicable.

Conflicts of Interest: The authors declare no conflict of interest.

References

1. Zhu, L.; Yuan, K.; Li, Z.; Miao, X.; Wang, J.; Sun, S.; Devi, A.; Lu, H. Highly sensitive and stable MEMS acetone sensors based on well-designed α-Fe_2O_3/C mesoporous nanorods. *J. Colloid Interface Sci.* **2022**, *622*, 156–168. [CrossRef] [PubMed]
2. Deng, L.; Bao, L.; Xu, J.; Wang, D.; Wang, X. Highly sensitive acetone gas sensor based on ultra-low content bimetallic PtCu modified $WO_3·H_2O$ hollow sphere. *Chin. Chem. Lett.* **2020**, *31*, 2041–2044. [CrossRef]
3. Lee, J.; Choi, Y.; Park, B.; Han, J.; Lee, H.; Park, J.; Lee, W. Precise control of surface oxygen vacancies in ZnO nanoparticles for extremely high acetone sensing response. *J. Adv. Ceram.* **2022**, *11*, 769–783. [CrossRef]
4. Ama, O.; Sadiq, M.; Johnson, M.; Zhang, Q.; Wang, D. Novel 1D/2D KWO/$Ti_3C_2T_x$ Nanocomposite-Based Acetone Sensor for Diabetes Prevention and Monitoring. *Chemosensors* **2020**, *8*, 102. [CrossRef]
5. Fanget, S.; Hentz, S.; Puget, P.; Arcamone, J.; Matheron, M.; Colinet, E.; Andreucci, P.; Duraffourg, L.; Myers, E.; Roukes, M.L. Gas sensors based on gravimetric detection—A review. *Sens. Actuators B* **2011**, *160*, 804–821. [CrossRef]
6. Liu, K.; Zhang, C. Volatile organic compounds gas sensor based on quartz crystal microbalance for fruit freshness detection: A review. *Food Chem.* **2021**, *334*, 127615. [CrossRef] [PubMed]
7. Avramov, I.D.; Ivanov, G.R. Layer by Layer Optimization of Langmuir–Blodgett Films for Surface Acoustic Wave (SAW) Based Sensors for Volatile Organic Compounds (VOC) Detection. *Coatings* **2022**, *12*, 669. [CrossRef]
8. Kanawade, R.; Kumar, A.; Pawar, D.; Vairagi, K.; Late, D.; Sarkar, S.; Sinha, R.K.; Mondal, S. Negative axicon tip-based fiber optic interferometer cavity sensor for volatile gas sensing. *Opt. Express* **2019**, *27*, 7277–7290. [CrossRef]
9. Dadkhah, M.; Tulliani, J. Nanostructured Metal Oxide Semiconductors towards Greenhouse Gas Detection. *Chemosensors* **2022**, *10*, 57. [CrossRef]
10. Deng, C.; Zhang, J.; Yu, X.; Zhang, W.; Zhang, X. Determination of acetone in human breath by gas chromatography–mass spectrometry and solid-phase microextraction with on-fiber derivatization. *J. Chromatogr. B* **2004**, *810*, 269–275. [CrossRef]
11. Galstyan, V.; Bhandari, M.P.; Sberveglieri, V.; Sberveglieri, G.; Comini, E. Metal Oxide Nanostructures in Food Applications: Quality Control and Packaging. *Chemosensors* **2018**, *6*, 16. [CrossRef]
12. Li, G.; Shen, Y.; Zhao, S.; Bai, J.; Gao, S.; Liu, W.; Wei, D.; Meng, D.; San, X. Construction of rGO-SnO_2 heterojunction for enhanced hydrogen detection. *Appl. Surf. Sci.* **2022**, *585*, 152623. [CrossRef]

13. Tao, K.; Han, X.; Yin, Q.; Wang, D.; Han, L.; Chen, L. Metal-Organic Frameworks-Derived Porous In$_2$O$_3$ Hollow Nanorod for High-Performance Ethanol Gas Sensor. *ChemistrySelect* **2017**, *2*, 10918–10925. [CrossRef]

14. Liu, M.; Song, P.; Zhong, X.; Yang, Z.; Wang, Q. Facile synthesis of Au-decorated α-Fe$_2$O$_3$/rGO ternary hybrid structure nanocomposites for enhanced triethylamine gas-sensing properties. *J. Mater. Sci. Mater. Electron.* **2020**, *31*, 22713–22726. [CrossRef]

15. Zhao, S.; Shen, Y.; Yan, X.; Zhou, P.; Yin, Y.; Lu, R.; Han, C.; Cui, B.; Wei, D. Complex-surfactant-assisted hydrothermal synthesis of one-dimensional ZnO nanorods for high-performance ethanol gas sensor. *Sens. Actuators B* **2019**, *286*, 501–511. [CrossRef]

16. Wang, X.; Han, W.; Yang, J.; Jiang, B.; Cheng, P.; Wang, Y.; Sun, P.; Zhang, H.; Sun, Y.; Lu, G. Facet effect on diverse WO$_3$ morphologies and ideal work function for ppb-level triethylamine detection. *Sens. Actuators B* **2022**, *363*, 131849. [CrossRef]

17. Gao, Y.; Chen, D.; Hou, X.; Zhang, Y.; Yi, S.; Ji, H.; Wang, Y.; Yin, L.; Sun, J. Microwave-assisted synthesis of hierarchically porous Co$_3$O$_4$/rGO nanocomposite for low-temperature acetone detection. *J. Colloid Interface Sci.* **2021**, *594*, 690–701. [CrossRef]

18. Bai, H.; Guo, H.; Wang, J.; Dong, Y.; Liu, B.; Xie, Z.; Guo, F.; Chen, D.; Zhang, R.; Zheng, Y. A room-temperature NO$_2$ gas sensor based on CuO nanoflakes modified with rGO nanosheets. *Sens. Actuators B* **2021**, *337*, 129783. [CrossRef]

19. Meng, D.; Qiao, T.; Wang, G.; San, X.; Meng, F. One-step synthesis of rGO/V$_2$O$_5$ flower-like microsphere composites with enhanced trimethylamine sensing properties. *Mater. Lett.* **2021**, *299*, 130023. [CrossRef]

20. Meng, F.; Qi, T.; Zhang, J.; Zhu, H.; Yuan, Z.; Liu, C.; Qin, W.; Ding, M. MoS$_2$-Templated Porous Hollow MoO$_3$ Microspheres for Highly Selective Ammonia Sensing via a Lewis Acid-Base Interaction. *IEEE Trans. Ind. Electron.* **2022**, *69*, 960–970. [CrossRef]

21. Choi, J.; Seo, J.; Jeong, H.; Song, K.; Baeck, S.; Shim, S.; Qian, Y. Effects of Field-Effect and Schottky Heterostructure on p-Type Graphene-Based Gas Sensor Modified by n-Type In$_2$O$_3$ and Phenylenediamine. *Appl. Surf. Sci.* **2022**, *578*, 152025. [CrossRef]

22. Liang, T.; Kim, D.; Yoon, J.; Yu, Y. Rapid synthesis of rhombohedral In$_2$O$_3$ nanoparticles via a microwave-assisted hydrothermal pathway and their application for conductometric ethanol sensing. *Sens. Actuators B* **2021**, *346*, 130578. [CrossRef]

23. Zhang, K.; Qin, S.; Tang, P.; Feng, Y.; Li, D. Ultra-sensitive ethanol gas sensors based on nanosheet-assembled hierarchical ZnO-In$_2$O$_3$ heterostructures. *J. Hazard. Mater.* **2020**, *391*, 122191. [CrossRef] [PubMed]

24. Zhang, W.; Ding, S.; Zhang, Q.; Yi, H.; Liu, Z.; Shi, M.; Guan, R.; Yue, L. Rare earth element-doped porous In$_2$O$_3$ nanosheets for enhanced gas-sensing performance. *Rare Met.* **2021**, *40*, 1662–1668. [CrossRef]

25. Huang, X.; Tang, Z.; Tan, Z.; Sheng, S.; Zhao, Q. Hierarchical In$_2$O$_3$ nanostructures for improved formaldehyde: Sensing performance. *J. Mater. Sci. Mater. Electron.* **2021**, *32*, 11857–11864. [CrossRef]

26. Kohli, N.; Hastir, A.; Kumari, M.; Singh, R.C. Hydrothermally synthesized heterostructures of In$_2$O$_3$/MWCNT as acetone gas sensor. *Sens. Actuators A* **2020**, *314*, 112240. [CrossRef]

27. Gupta Chatterjee, S.; Chatterjee, S.; Ray, A.; Chakraborty, A. Graphene–metal oxide nanohybrids for toxic gas sensor: A review. *Sens. Actuators B* **2015**, *221*, 1170–1181. [CrossRef]

28. Liu, X.; Liu, J.; Liu, Q.; Chen, R.; Zhang, H.; Yu, J.; Song, D.; Li, J.; Zhang, M.; Wang, J. Template-free synthesis of rGO decorated hollow Co$_3$O$_4$ nano/microspheres for ethanol gas sensor. *Ceram. Int.* **2018**, *44*, 21091–21098. [CrossRef]

29. Ren, H.; Gu, C.; Joo, S.W.; Zhao, J.; Sun, Y.; Huang, J. Effective hydrogen gas sensor based on NiO@rGO nanocomposite. *Sens. Actuators B* **2018**, *266*, 506–513. [CrossRef]

30. de Lima, B.; Komorizono, A.; Ndiaye, A.; Bernardi, M.B.; Brunet, J.; Mastelaro, V. Tunning the Gas Sensing Properties of rGO with In$_2$O$_3$ Nanoparticles. *Surfaces* **2022**, *5*, 127–142. [CrossRef]

31. Dong, X.; Han, Q.; Kang, Y.; Li, H.; Huang, X.; Fang, Z.; Yuan, H.; Elzatahry, A.A.; Chi, Z.; Wu, G.; et al. Rational construction and triethylamine sensing performance of foam shaped α-MoO$_3$@SnS$_2$ nanosheets. *Chin. Chem. Lett.* **2022**, *33*, 567–572. [CrossRef]

32. Liu, J.-B.; Hu, J.-Y.; Liu, C.; Tan, Y.-M.; Peng, X.; Zhang, Y. Mechanically exfoliated MoS$_2$ nanosheets decorated with SnS$_2$ nanoparticles for high-stability gas sensors at room temperature. *Rare Met.* **2021**, *40*, 1536–1544. [CrossRef]

33. Meng, F.; Li, X.; Yuan, Z.; Lei, Y.; Qi, T.; Li, J. Ppb-Level Xylene Gas Sensors Based on Co$_3$O$_4$ Nanoparticle-Coated Reduced Graphene Oxide(rGO) Nanosheets Operating at Low Temperature. *IEEE Trans. Instrum. Meas.* **2021**, *70*, 1–10. [CrossRef]

34. Hung, C.; Dat, D.; Van Duy, N.; Van Quang, V.; Van Toan, N.; Van Hieu, N.; Hoa, N. Facile synthesis of ultrafine rGO/WO$_3$ nanowire nanocomposites for highly sensitive toxic NH$_3$ gas sensors. *Mater. Res. Bull.* **2020**, *125*, 110810. [CrossRef]

35. Lin, G.; Wang, H.; Lai, X.; Yang, R.; Zou, Y.; Wan, J.; Liu, D.; Jiang, H.; Hu, Y. Co$_3$O$_4$/N-doped RGO nanocomposites derived from MOFs and their highly enhanced gas sensing performance. *Sens. Actuators B* **2020**, *303*, 127219. [CrossRef]

36. Zuo, J.; Tavakoli, S.; Mathavakrishnan, D.; Ma, T.; Lim, M.; Rotondo, B.; Pauzauskie, P.; Pavinatto, F.; MacKenzie, D. Additive Manufacturing of a Flexible Carbon Monoxide Sensor Based on a SnO$_2$-Graphene Nanoink. *Chemosensors* **2020**, *8*, 36. [CrossRef]

37. Cao, P.; Cai, Y.; Pawar, D.; Navale, S.; Rao, C.; Han, S.; Xu, W.; Fang, M.; Liu, X.; Zeng, Y.; et al. Down to ppb level NO$_2$ detection by ZnO/rGO heterojunction based chemiresistive sensors. *Chem. Eng. J.* **2020**, *401*, 125491. [CrossRef]

38. Mishra, R.K.; Murali, G.; Kim, T.-H.; Kim, J.H.; Lim, Y.J.; Kim, B.-S.; Sahay, P.P.; Lee, S.H. Nanocube In$_2$O$_3$@RGO heterostructure based gas sensor for acetone and formaldehyde detection. *RSC Adv.* **2017**, *7*, 38714–38724. [CrossRef]

39. Hummers, W.; Offeman, R. Preparation of Graphitic Oxide. *J. Am. Chem. Soc.* **1958**, *80*, 1339. [CrossRef]

40. Yang, W.; Wan, P.; Zhou, X.; Hu, J.; Guan, Y.; Feng, L. Additive-Free Synthesis of In$_2$O$_3$ Cubes Embedded into Graphene Sheets and Their Enhanced NO$_2$ Sensing Performance at Room Temperature. *ACS Appl. Mater. Interfaces* **2014**, *6*, 21093–21100. [CrossRef]

41. White, J.; Bocarsly, A. Enhanced Carbon Dioxide Reduction Activity on Indium-Based Nanoparticles. *J. Electrochem. Soc.* **2016**, *163*, H410–H416. [CrossRef]

42. Zhang, Q.; Wang, S.; Fu, H.; Wang, Y.; Yu, K.; Wang, L. Facile Design and Hydrothermal Synthesis of In$_2$O$_3$ Nanocube Polycrystals with Superior Triethylamine Sensing Properties. *ACS Omega* **2020**, *5*, 11466–11472. [CrossRef] [PubMed]

43. Yang, W.; Feng, L.; He, S.; Liu, L.; Liu, S. Density Gradient Strategy for Preparation of Broken In$_2$O$_3$ Microtubes with Remarkably Selective Detection of Triethylamine Vapor. *ACS Appl. Mater. Interfaces* **2018**, *10*, 27131–27140. [CrossRef] [PubMed]

44. Rodwihok, C.; Wongratanaphisan, D.; Thi Ngo, Y.; Khandelwal, M.; Hur, S.; Chung, J. Effect of GO Additive in ZnO/rGO Nanocomposites with Enhanced Photosensitivity and Photocatalytic Activity. *Nanomaterials* **2019**, *9*, 1441. [CrossRef]

45. Yu, L.; Wan, G.; Peng, X.; Dou, Z.; Li, X.; Wang, K.; Lin, S.; Wang, G. Fabrication of carbon-coated NiO supported on graphene for high performance supercapacitors. *RSC Adv.* **2016**, *6*, 14199–14204. [CrossRef]

46. Yan, H.; Song, P.; Zhang, S.; Zhang, J.; Yang, Z.; Wang, Q. Au nanoparticles modified MoO$_3$ nanosheets with their enhanced properties for gas sensing. *Sens. Actuators B* **2016**, *236*, 201–207. [CrossRef]

47. Liu, B.; Zhu, Q.; Pan, Y.; Huang, F.; Tang, L.; Liu, C.; Cheng, Z.; Wang, P.; Ma, J.; Ding, M. Single-Atom Tailoring of Two-Dimensional Atomic Crystals Enables Highly Efficient Detection and Pattern Recognition of Chemical Vapors. *ACS Sens.* **2022**, *7*, 1533–1543. [CrossRef]

48. Chaloeipote, G.; Prathumwan, R.; Subannajui, K.; Wisitsoraat, A.; Wongchoosuk, C. 3D printed CuO semiconducting gas sensor for ammonia detection at room temperature. *Mater. Sci. Semicond. Process.* **2021**, *123*, 105546. [CrossRef]

49. Chang, X.; Li, K.; Qiao, X.; Xiong, Y.; Xia, F.; Xue, Q. ZIF-8 derived ZnO polyhedrons decorated with biomass derived nitrogen-doped porous carbon for enhanced acetone sensing. *Sens. Actuators B* **2021**, *330*, 129366. [CrossRef]

50. Qin, Q.; Zhu, X.; Zhang, X. Synthesis of α-Fe$_2$O$_3$ hollow spheres with rapid response and excellent selectivity towards acetone. *Mater. Sci. Eng. B* **2022**, *275*, 115482. [CrossRef]

51. Zhu, H.; Haidry, A.A.; Wang, Z.; Ji, Y. Improved acetone sensing characteristics of TiO$_2$ nanobelts with Ag modification. *J. Alloys Comp.* **2021**, *887*, 161312. [CrossRef]

52. Wang, G.; Fu, Z.; Wang, T.; Lei, W.; Sun, P.; Sui, Y.; Zou, B. A rational design of hollow nanocages Ag@CuO-TiO$_2$ for enhanced acetone sensing performance. *Sens. Actuators B* **2019**, *295*, 70–78. [CrossRef]

53. Wang, Q.; Cheng, X.; Wang, Y.; Yang, Y.; Su, Q.; Li, J.; An, B.; Luo, Y.; Wu, Z.; Xie, E. Sea urchins-like WO$_3$ as a material for resistive acetone gas sensors. *Sens. Actuators B* **2022**, *355*, 131262. [CrossRef]

54. Cheng, P.; Wang, C.; Wang, Y.; Xu, L.; Dang, F.; Lv, L.; Li, X. Enhanced acetone sensing properties based on in situ growth SnO$_2$ nanotube arrays. *Nanotechnology* **2021**, *32*, 245503. [CrossRef]

55. Ueda, T.; Boehme, I.; Hyodo, T.; Shimizu, Y.; Weimar, U.; Barsan, N. Enhanced NO$_2$-Sensing Properties of Au-Loaded Porous In$_2$O$_3$ Gas Sensors at Low Operating Temperatures. *Chemosensors* **2020**, *8*, 72. [CrossRef]

56. Gu, D.; Liu, W.; Wang, J.; Yu, J.; Zhang, J.; Huang, B.; Rumyantseva, M.N.; Li, X. Au Functionalized SnS$_2$ Nanosheets Based Chemiresistive NO$_2$ Sensors. *Chemosensors* **2022**, *10*, 165. [CrossRef]

57. Lv, L.; Cheng, P.; Zhang, Y.; Zhang, Y.; Lei, Z.; Wang, Y.; Xu, L.; Weng, Z.; Li, C. Ultra-high response acetone gas sensor based on ZnFe$_2$O$_4$ pleated hollow microspheres prepared by green NaCl template. *Sens. Actuators B* **2022**, *358*, 131490. [CrossRef]

58. Nakate, U.T.; Yu, Y.T.; Park, S. High performance acetaldehyde gas sensor based on p-n heterojunction interface of NiO nanosheets and WO$_3$ nanorods. *Sens. Actuators B* **2021**, *344*, 130264. [CrossRef]

59. Wan, K.; Wang, D.; Wang, F.; Li, H.; Xu, J.; Wang, X.; Yang, J. Hierarchical In$_2$O$_3$@SnO$_2$ Core-Shell Nanofiber for High Efficiency Formaldehyde Detection. *ACS Appl. Mater. Interfaces* **2019**, *11*, 45214–45225. [CrossRef]

60. Qiu, Y.; Wang, Y.; Song, C. Facile synthesis of W$_{18}$O$_{49}$/Graphene nanocomposites for highly sensitive ethanol gas sensors. *Colloids Surf. A* **2021**, *616*, 126300. [CrossRef]

61. Cheng, M.; Wu, Z.; Liu, G.; Zhao, L.; Gao, Y.; Zhang, B.; Liu, F.; Yan, X.; Liang, X.; Sun, P.; et al. Highly sensitive sensors based on quasi-2D rGO/SnS$_2$ hybrid for rapid detection of NO$_2$ gas. *Sens. Actuators B* **2019**, *291*, 216–225. [CrossRef]

62. Bai, S.; Tian, K.; Zhao, Y.; Feng, Y.; Luo, R.; Li, D.; Chen, A. ZnO/BiFeO$_3$ heterojunction interface modulation and rGO modification for detection of triethylamine. *J. Mater. Chem. C* **2022**, *10*, 8015–8023. [CrossRef]